https://doi.org/10.48048/tis.2024.7221

Application of ERT, IP and VLF-EM Methods to Investigate Landslide-Prone Structures at Archaeological Sites in Lamreh, Aceh Besar, Indonesia

Bukhari Ali[1,2], Muhammad Nanda[3,4], Muzakir Zainal[5], Muhammad Yanis[4,5], Muhammad Syukri Surbakti[2], Nasrullah Idris[2] and Nazli Ismail[2,4,5,*]

[1]Graduate School of Mathematics and Applied Sciences, Universitas Syiah Kuala, Banda Aceh 23111, Indonesia
[2]Department of Physics, Universitas Syiah Kuala, Banda Aceh 23111, Indonesia
[3]Department of Marine Sciences, Faculty of Marine and Fisheries, Universitas Syiah Kuala, Banda Aceh 23111, Indonesia
[4]Research Center Ethnosciences, Universitas Syiah Kuala, 23111, Darussalam, Banda Aceh, Indonesia
[5]Geophysical Engineering Department, Universitas Syiah Kuala, Banda Aceh 23111, Indonesia

([*]Corresponding author's e-mail: nazli.ismail@usk.ac.id)

Received: 18 June 2023, Revised: 26 July 2023, Accepted: 1 August 2023, Published: 30 January 2024

Abstract

Since the 21st century, Lamreh, Aceh Besar Regency, Indonesia played an important role during the maritime silk route at the gate of the Malacca strait. This article investigates the subsurface structure of landslide-prone areas in cultural heritage based on 2D resistivity, chargeability and current density models of ERT, IP and VLF-EM methods, respectively. Field data measurements were carried out on 2 crossing profiles along the cliff suspected of experiencing landslides. The length of each profile is 220 with 4 m distance between stations. The 2D models reveal that the subsurface geological structure of Lamreh is composed of a mixed layer of clastic sediment and volcanic material at the top, followed by a layer of calcareous sandstone, and volcanic breccia at the bottom. The 3 layers are most easily distinguished in the resistivity model. The topmost layer is permeable but dry, i.e., characterized by a more resistive layer in the models. While the second layer is characterized by an intermediate conductivity and the bottom layer is highly conductive. The conductivity in these 2 layers is influenced by the degree of water content within the rocks. The chargeability models derived from IP data can distinguish between the dry layer on the surface and the saturated layer below. Meanwhile, the current density models obtained from VLF-EM data have proven the presence of fractures and faults along the profiles due to weathering as also seen in the resistivity models.

Keywords: Resistivity, Chargeability, Current density, Disaster mitigation, Cultural heritage

Introduction

The maritime trade silk route left archaeological evidence in Lamreh village, a hilly area on the northern Sumatra (**Figure 1**). In the past, the village was known as Lamuri, the gate of shipping from the west to Southeast Asia through the Malacca Strait [1-5]. Many archaeological remains such as building structures, ceramic shards and gravestones in the area. The shapes and motifs of the gravestones are distinctive representing a certain period [6-11]. Distribution of ancient ceramic shards around the area helped some findings, e.g., paleotsunami evidence and ceramic trade ban of the Ming and Qing dynasty in Southeast Asia [10,12-15].

In the 15th century, the Portuguese also built the Kuta Lubok fort on the west side of Lamreh [16]. However, Lamuri has been known since the 9th century [17-19]. The toponym Lamuri was pronounced as *Lan-wu-li* in Chinese manuscripts. Since the 9th century Arabs called Lamuri as *Rami*, *Ramni* or *Lamri*. The 1,030 Tamil document from Thanjavur revealed Lamuri as *Ilamuridessam*. Odoric de Pordenone, an Italian late-medieval explorer and Marcopolo noted that Lamuri was a settlement in the late 13th century. Lamuri was also written in Nagara-Kertagama, an ancient Javanese manuscript in 1365. In the 15th century, the largest maritime expedition of the Ming Dynasty in Southeast Asia called Lamuri as *Nan-po-li*. The 17th century Armenian manuscripts mentioned that Lamuri was a coastal region of Aceh in the early 15th century.

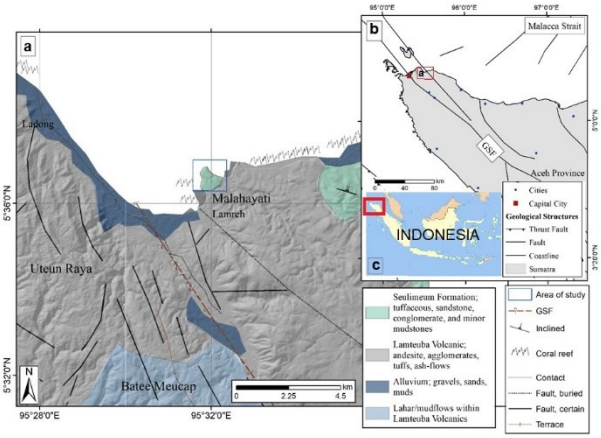

Figure 1 Location of the study area in the geological map of Aceh Besar [20], a) The Lambaro headland is shown inside the blue rectangle, b) Tectonic setting of the northwest of Sumatra in c) Indonesia.

Today, Lamuri is just recognized as a village, called Lamreh, with approximately 88.6 square hectares located in Masjid Raya sub-district, Aceh Besar Regency, Aceh Province, Indonesia. The village is situated 30 km to the east of Banda Aceh, the capital of Aceh Province (**Figure 1**). Lamreh area is also known as Lambaro headland [12] surrounded by a cliff with a height of about 35 m above MSL. The meeting between the Straits of Malacca, the Bay of Bengal and the Indian Ocean causes a unique hydrodynamics system in the region [21]. The very steep cliff occurred due to a continuous erosional process which is vulnerable to landslide hazards [22].

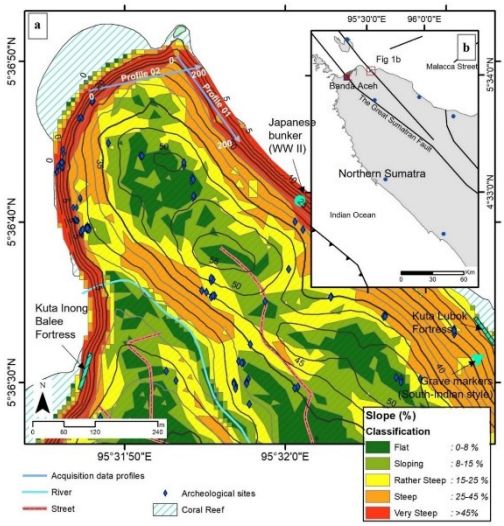

Figure 2 a) Slope and contour map of the study area and b) tectonic setting of the northwest of Sumatra. The distribution of old gravestones is shown in blue diamonds. The locations of profile 1 and profile 2 are represented by 2 crossing solid blue lines at the northwest of the headland.

The Lamreh area is rich in artifacts such as forts, buried structures, gravestones and ceramics shards (**Figure 2(a)**). Based on types and materials the ceramics originated from local and around the world. In the area, found about 200 ancient *plang-pleng* gravestones [11]. The gravestones were made of sandstone and andesite carved with floral ornaments and Arabic inscriptions. The 2 existing noticed buildings in the area are the Inong Balee fort (built in 1599) on the west side and the Kuta Lubok fort in a valley on the east side of Lamreh. A Japanese bunker from the Second World War is also found there.

To protect the archaeological area from landslides, mitigation efforts need to be carried out. Preventing landslides can be done by geotechnical engineering, for example, slope geometry modification or piles and retaining walls e.g., [23,24]. Therefore, it is necessary to characterize the subsurface structure of the area so that the applied technique works effectively.

The prone landslide areas can be identified by observing the slope of the land or interpreting aerial images. However, a landslide mostly occurs in complex geological subsurface structures. Geological conditions, weathering and erosional processes, rainfall, hydrological conditions and human activities [25]. The main causes that can trigger landslides are related to the near-surface conditions of the structures and the hydrology of the area which has the potential for landslides [26]. Information about changes in the physical properties of subsurface material with depth, depth of water table, slope and depth of the sliding surface need to be characterized before landslide mitigation is carried out. The application of geophysical methods is believed to be able to investigate such information with fast, reliable and costly effectiveness.

Geophysical methods have been widely used to investigate land that has the potential for landslides [27-30]. However, the electrical properties of rock material are strongly influenced by the presence of water within it. The electrical resistivity tomography (ERT) method is reliable in resolving shallow subsurface models based on the electrical properties of the material. For landslide investigation, the geoelectrical method was first introduced by [31]. The ERT method can resolve subsurface structures in 2D and 3D models e.g., [27,33,34], and hydrological monitoring e.g., [29,30,34,35] so that it can identify changes in ground movement with spatial-temporal variations.

On the other hand, the induced polarization (IP) method is based on variations in the electrical chargeability of the material [36]. The method has been applied to explore hydrogeological properties e.g., [37] and to predict soil water content and cation exchange capacities e.g., [38,39]. A combination of the 2 methods will be able to provide a better image of the subsurface structures [36,40,41].

The very low frequency electromagnetic (VLF-EM) uses electromagnetic waves transmitted by ground-based military radio in a range of frequency 15 - 30 kHz. The VLF-EM method can be operated by only 1 person [42] and collected the data faster than ERT or IP methods [43]. The challenge using the VLF method is unstable transmitters with blank signals due to specific area and time duration [44,45]. The 2D VLF method has been used to investigate landslide areas [46], the erosional area around a cultural heritage [47], water seepage [48] and near-surface fault structures [49-50].

This paper discusses the reliability of the ERT, IP and VLF-EM methods in modeling the subsurface structure of the landslide-prone area in the Lamreh cultural heritage. Geophysical studies in the Lamreh area are still limited [22,47], but history and archaeological studies are widely available because of the importance of this cultural heritage site [1-8,10-15,17,19,51]. Because of its position facing the Malacca Strait, the scenery on the hills of Lamreh attracts tourists. The local government had planned to develop the area for a golf course [52]. The Lamreh heritage site will not only be prone to landslides but also the threat of land conversion. Therefore, studies concerning the importance of the Lamreh heritage area need to be encouraged. This paper will enrich references on the Lamreh heritage for conservation. The ERT, IP and VLF-EM methods were used in this study because of their non-destructive nature. The VLF-EM method uses electromagnetic waves, while the source current injected in the ERT and IP methods has no significant effect on the environment.

Methods

Study area description

Lamreh village is located about 30 km to the east of Banda Aceh, the capital of Aceh Province (**Figure 1(b)**) which is also known as Lambaro headland at the northernmost part of the Barisan Mountains. The Barisan mountain lined up on the western side of Sumatra consists primarily of volcanoes. The Lambaro headline is flanked by 2 active volcanoes, Seulawah Agam volcano at the south and Weh volcano located on Weh Island at the north [53]. Regional geological setting the northern part of the Barisan mountains is underlain by rocks of Jurassic to Cretaceous age and Quaternary volcanic rocks overlie the basement rocks [20]. The Great Sumatran Fault (GSF) also passes through this area on the west side (**Figure 1**). The GSF runs along Sumatra Island in a direction almost NW-SE. Being surrounded by volcanoes and an active fault system makes the local geological setting unique.

The Lambaro headland lies between 2 valleys, on the east and west coasts of the headland found a small alluvial fan that contains evidence of marine inundation. The alluvial fan consists predominantly of debris from volcanic breccia and calcareous beds, washed down from the surrounding hills [12]. On the west coast is a small valley filled by alluvial nestled between low hills and truncated at a low sea cliff. A local dipping fault of volcanic breccias is well visible in the sea cliffs that flank the valley. On top of these layers, calcareous sand and massive limestone breccia are deposited. Approximately north and south of the valley, these beds underlie gentle surfaces about 20 m above sea level [12]. The area may be uplifted by the movement of the strike-slip Sumatran fault that crosses not far away from the west side of Lamreh at a rate of 0.1 mm/year [54]. While the hydrogeology of Lamreh is influenced by the tropical climate. The

highest rainfall usually occurs in November and December and the peak of the dry season is in June and July. The average annual rainfall in the Aceh Besar area is 1,500 mm/year. The hydrology of the area is governed by equatorial convective and monsoonal rainfalls [55].

Slope calculation

Site selection for ERT, IP and VLF-EM 2D data acquisition was referred to as field observations and land slope maps. The slope parameter is one of the main factors in hydro geomorphological studies [58,59]. Digital elevation model (DEM) data derived from DEMNAS with a resolution of 0.27 arc-second [62] were used to calculate the slope [60] as shown in Eq. (1).

$$Slope = \arctan\left[\sqrt{x^2 + y^2}\right], \quad (1)$$

where x and y values are in the x- and y-directions of the DEM data. Small slope values indicate a flat surface and higher slope values indicate a steep surface [64].

Geophysical data acquisition

Three geophysical methods, namely ERT, IP and VLF-EM, were applied for imaging subsurface structures of the landslide-prone area. The ERT method relies on contrasting electrical properties of the material, penetration depth and resolution [62]. During measurement, an electrical current (I) is inserted into the ground with 2 current electrodes, and measuring the electrical potential difference (ΔV) uses 2 potential electrodes on the surface. The electrical resistivity variation within the subsurface can be imaged when there is a contrast in electrical properties between targeted objects and their surroundings. The apparent resistivity (ρ_a) of the subsurface in the heterogeneous media is obtained by Eq. (2).

$$\rho_a = k\frac{\Delta V}{I} \quad (2)$$

The k parameter is a geometric factor based on electrode configurations applied. Wenner electrode configuration has been applied in this measurement. For 1D measurement, so-called vertical electrical sounding (VES), the Wenner electrode configuration uses 4 electrodes in line with the same space distant between each electrode. The first and the 4 electrodes function as current electrodes and the second and the third electrodes in between the current electrodes are used as potential electrodes. The depth penetration of the measurement can be increased by increasing the distance between the electrodes, but the center point of the configuration is the same for all measurements. For 2D profiling, horizontal changes of resistivity can be investigated by shifting the 4 electrodes along the profile measurement by maintaining constant electrode separation. By using multielectrode equipment, both measurements can be performed simultaneously.

The geometry of the ERT data measurement is also valid for the Induced Polarization (IP) method. The IP method is sensitive to capacity properties of material, i.e., the ability of material to store reversibly electrical charges with an external electrical field. The relaxation time needed by these charges revert to equilibrium after the electrical field is applied [39]. By inserting an electrical current flow through the 2 electrodes, a primary potential difference (ΔV_p) is generated. The potential difference varies with time and acquires the shape of a curve (ΔV_{IP}) as a function of time. This curve fixed the steady-state asymptote ΔV_p with 0 asymptotes after the current was removed. The amplitude of a $\Delta V_{IP}(t)$ value is related to the subsurface material's capacity to polarize. The time domain IP method measures chargeability (M) in a millisecond.

$$M = \frac{1}{V_P}\int_{t_1}^{t_2} \Delta V_{IP}(t)dt \quad (3)$$

In the VLF data acquisition, the instrument measures the total magnetic field (H_R), i.e., the primary (H_P) from the radio transmitters and the second field (Hs) as the magnetic field induced by the conductor within the earth. The magnitude of Hs and H_R depends on space, time and frequency [63]. The measured fields will have a different phase (φ) between the primary and secondary fields, i.e.:

$$H_R = |H_p|e^{iwt} + |H_s|e^{i(wt-\varphi)}, \quad (4)$$

Denotations ω and t represent angular frequency and time, respectively. The VLF-EM instrument measures the vertical component **(***Hz***)** and horizontal **(***Hy***)** of the magnetic field.

Fraser [64] and Karous Hjelt filters (KHFfilt) are standard filtering techniques for qualitative analysis of VLF-EM data. The Fraser filter changes the point of in-phase and out-phase data into a maximum response by shifting to 90 °. The cross-section between both data shows the anomaly position. The basic principle of the Fraser is used in phase or out-phase data from 4 stations by subtracting the data from the 3rd and 4th to the 1st and 2nd stations as:

$$F_{2,3} = (H3 + H4) - (H1 + H2) \quad (4)$$

A relative conductivity filter can be used to explain subsurface anomalies based on conductivity parameters [65]. Karous-Hjelt is a VLF filter developed based on the Biot-Savart law to describe the vertical component of magnetic fields associated with electric currents. The filter generates a depth profile of the electric density in each station by:

$$\left(\frac{\Delta z}{2\pi}\right) I_a \left(\frac{\Delta x}{2}\right) = -0.205\, H_{-2} + 0.323\mathrm{H}_{-1} - 1.446 H_0 + 1446 H_1 - 0.323 H_2 + 0.205\, H_3\, I_a(x/2), \quad (5)$$

Δz is the thickness assumption for the cross-sectional area of charge density, Δx is the distance between stations as the depth in a layer. At the same time, the *H2* to *H3* values are the vertical magnetic field (*Hz*/*Hy*) in the 6-measurement data [66]. This filter indicates electric current depth due to subsurface responses, such as fault and fracture zones.

Field data measurements of ERT, IP and VLF-EM were collected along 2 crossing profiles in northwest-southeast (Profile 1) and slightly southwest-northeast (Profile 2) directions. The 2 profiles intersect on the west side of the cliff in the north (**Figure 2(a)**). The ERT and IP data were acquired using unit Supersting R8/IP 56 Electrode Electric Resistivity spacing of 4 with 220 m long each profile. The maximum depth reached from the inversion model of ERT and IP is up to 50 m. To resolve the lateral and vertical resolution of the subsurface, the Wenner electrode configuration was installed during the ERT and IP measurement [67]. A time domain survey was conducted in the IP measurement by injecting current and measuring voltage decay over time [68]. Both the 2D resistivity and chargeability models were inverted using the RES2DINV software. The inversion model used in this paper is based on the smoothness-constrained least-squares inversion method. [69]. The VLF-EM data was collected using a GSM 19 instrument. The data at each station were measured simultaneously with frequencies of 19.8 and 21.4 kHz transmitted from Western Australia and Hawaii, respectively [70,71].

Results and discussion

The slope map of the area was calculated based on Eq. (1) as presented in **Figure 2(a)**. The slope ranges were classified into flat, intermediate and steep surfaces [72]. The flat category (0 - 8 %) comprises 21.7 % and the steepest category (< 45 %) covers 6 % of the total area. The intermediate and steepest surfaces are found along the sea cliff. Areas with a slope gradient high potentially trigger landslides [56]. The steeper the slope the more vulnerable to instability [73]. The slope map in **Figure 2** shows that the area along the coastline is strongly influenced by land instability with categories steep to very steep [74]. Such slope failures may occur repeatedly and continue to threaten future landslides [58]. Based on these findings, measurements of ERT, IP and VLF-EM data were carried out in the northwest, where the slope is very steep.

The inverted models of ERT, IP and VLF-EM data are shown in **Figure 3**. The Root Mean Square (RMS) values for the inverted models of ERT are 2.87 and 2.48 %, respectively. As for the inverted models of IP, the RMS values are 8.68 and 9.57 msec, respectively. The 2 profiles of each method were combined in a 3D perspective. Dashed and red slash lines were added to the models to show interpreted boundary layers and locations of faults or fractures, respectively. The ERT and IP models have the same scale while the VLF-EM models show up to 30 m depth.

The ERT models of both profiles show 3 resistivity layers, from the most resistive on the top to the most conductive on the bottom (**Figure 3(a)**). The uppermost layer has resistivity values above 400 or 2.6 ohm-m in a logarithmic scale. The topmost resistive layer covers have an average thickness of about 15 m along profile 1. From a distance of 100 to 200 m, the resistive layer is relatively flat following the topography slope (**Figure 2(a)**). While at the northwest side, from a distance of 0 to 100 m, both the topography and the resistive layer are tilted. This also occurs on the other side of profile 1. The resistive

layer is sharply cut with a slope to the southeast from a distance of 180 m to the end of profile 1. It is expected that the sloping uppermost layer on both sides of the profile experienced landslides.

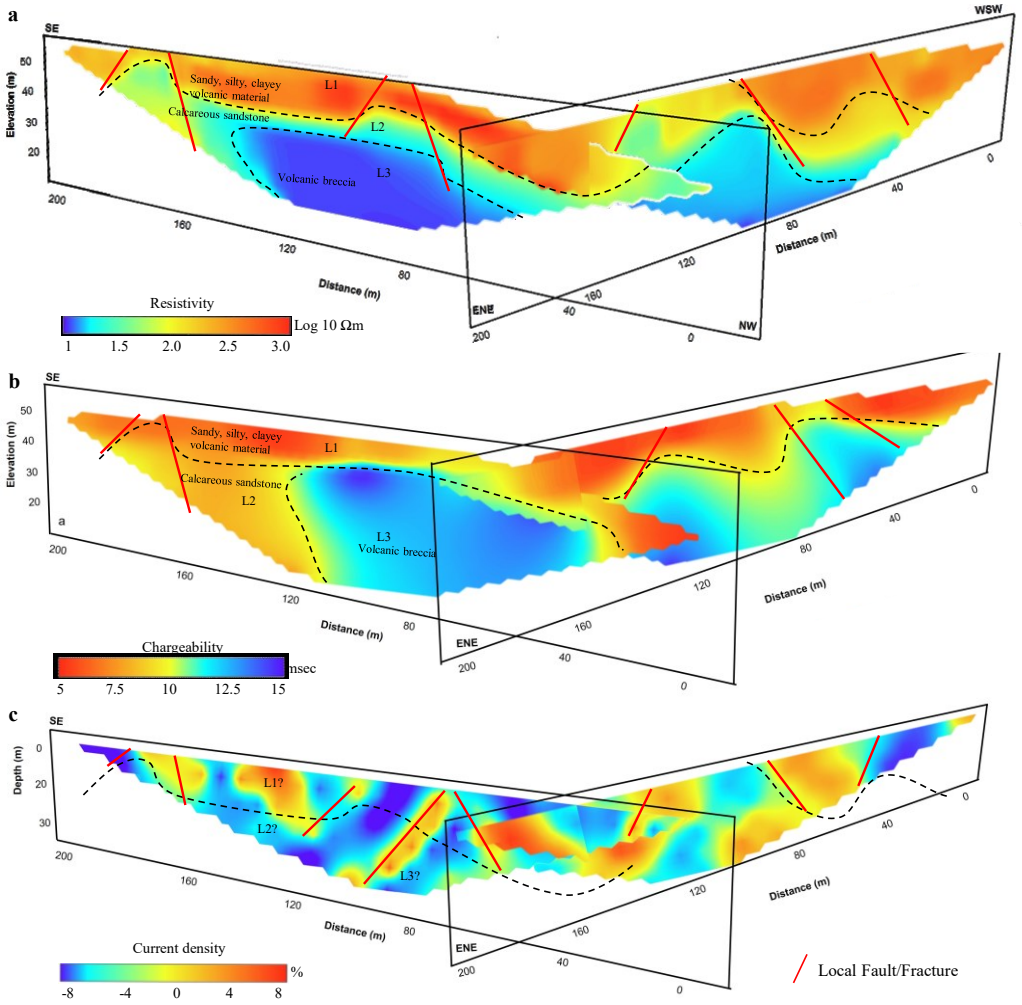

Figure 3 a) 3D views of 2D resistivity, b) chargeability and c) current density models inverted from ERT, IP and VLF-EM data, respectively. The profiles are viewed from the north. The dashed lines show boundaries between layers and the solid red slash lines show locations of expected local faults or fractures.

This topmost resistive layer rests on an intermediate resistivity values layer ranging from 20 to 400 ohm-m (1.3 to 2.6 ohm-m on a logarithmic scale). The thickness of the intermediate resistivity layer varies along the profile, but it drops sharply at a distance of 110 to 150 m in the middle of the profile to only a few meters. At a distance of 150 m to the southeast end of the layer profile, only the intermediate resistivity is imaged in the model. The bottom layer is very conducive with resistivity values less than 20 ohm-m (1.3 ohm-m on a logarithmic scale). The boundary between the intermediate resistivity layer and the conductive layer is very steep at a distance of 140 m. In the southeast, there is only an intermediate resistivity layer, while in the northwest there is only a highly conductive layer.

The resistivity model inverted from the ERT data in profile 2 agrees with the model in profile 1. However, the resistivity layers in profile 2 look a bit undulating compared to the layers in profile 1. The uppermost resistive layer is only found in the WSW section from 0 to 100 and from 150 m to the end of the profile next to the ENE. The resistive layer looks like it fills the basins formed in the intermediate resistivity layer below it. From 100 to 150 m, the intermediate resistivity layer appears near the surface. The undulations of the first and second layers follow the shape of a highly conductive bottom layer which is tilted towards WSW and ENE. This can be interpreted that landslide were taking place in each direction of the cliff sides.

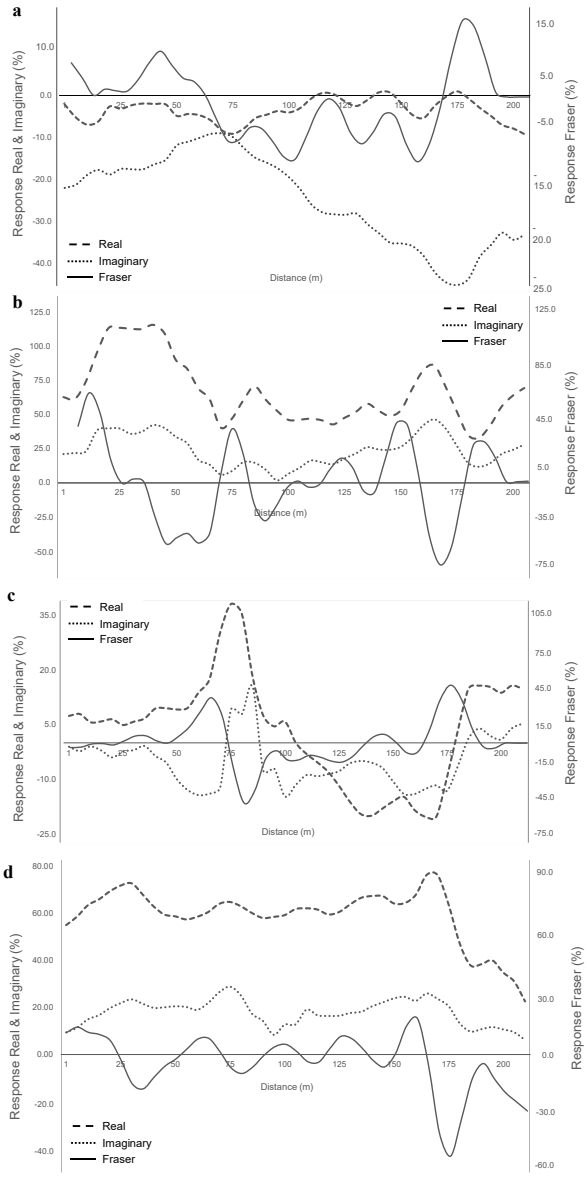

Figure 4 Real and imaginary components superimposed with Fraser filter of VLF-EM data from a) Profile 1 at frequency 19.8 and b) 21.4 kHz and c) Profile 2 at frequency 19.8, and d) 21.4 kHz.

The resistivity models generated from the ERT data are also well confirmed with the chargeability models extracted from the IP measurement data in both profiles, especially from the geometry of the layers (**Figure 3(b)**). Two dipping structures to the northwest along profile 1 are visible in both models. Likewise, the undulating layer structure along profile 2 is also clearly imaged in the resistivity and chargeability models. However, the IP models cannot distinguish clearly the 3 resistivity layers imaged by the ERT models, since each method has different sensitivity in the electrical properties of materials. The IP models are presented as normalized chargeability (msec). The top, intermediate, and bottom layers of IP models have chargeability values from 5 to 7.5, 10 to 12.5 and 12.5 to 15 msec, respectively.

For the VLF-EM models, we have examined the row data before modeling since the data can be influenced by noises from the secondary fields due to the presence of metals, power lines or topographic differences around the area [75]. However, the moving average window method can be used to improve data smoothing. **Figure 4** shows real (in-phase) and imaginary (out-phase) components of VLF-EM data collected along profile 1 at frequency 19.8 (**Figure 4(a)**) and 21.4 kHz (**Figure 4(b)**) and profile 2 at frequency 19.8 (**Figure 4(c)**) and 21.4 kHz (**Figure 4(d)**).

The in-phase and out-phase components of VLF-EM can be used for preliminary qualitative data interpretation. For example, cross-overs in the in-phase and out-phase profiles possibly indicate a geological body, depression zone or fault [76,77]. At frequency 19.8 kHz along profile 1 and profile 2, the in-phase and out-phase components crossover at some distances indicating vertical changes within the subsurface. Although it is not seen in the frequency of 21.4 kHz, the variation of both components along the profiles changes consistently (**Figures 4(b) - 4(d)**). Maximum and minimum values of the in-phase are followed by the out-phase components.

In addition, the Fraser filtering is also used for qualitative interpretation [64]. Maximum values of the Fraser filtered can be used to locate a conductor. The intensity and sharpness of the amplitude o can be interpreted as shallow and deep conductors, while low values correspond to resistive structures [78]. The location of the amplitudes along the profiles corresponds to the position of the vertical change of each layer in the resistivity models of the ERT method indicating the presence of fractures or faults. To be more comparable with ERT data resistivity models, it is necessary to calculate the current density models of VLF-EM data using Eq. (6) [79]. Only data measured at a frequency of 21.4 kHz are presented here for further discussion.

Variations of current density models with depth along profile 1 and profile 2 are shown in **Figure 4(c)**. The topography of the area was not incorporated in the calculated models. However, both profiles are in agreement with other models derived from ERT and IP data. The current density models show more simple features than the others VLF-EM data. The current density has a linear relationship with conductivity. The models show the area with low (negative) and high (positive) current density values. The positive values of current density can be related to a relatively high conductivity area probably caused by fault or fracture zones. Water content inside the porosity rocks increases the conductivity of the material. The resistivity models of the 2 profiles agree. The profiles intersect at a distance of 40 and 180 m along profile 1 and profile 2, respectively. This finding confirms that the 3 models are well-calibrated.

Figure 5 Photographs of different soil and rock units exposed on each side of the sea cliff. a) end side of profile 1, b) side of profile 1 that intersects with profile 2, c) ends side of profile 2 and d) side of profile 2 that intersects with profile 1. Note, humans are used as scales.

Previous geological studies and some outcrops found along the sea cliff (**Figure 5**) reveal that the uppermost layer of the area consists of sandy, silty and clayey with volcanic material and calcareous pebbles, cobbles and small boulders. The materials are loosely consolidated with high permeability. The very high resistivity values in the uppermost layer are caused by the material on the surface being very dry. Note that the measurements were carried out in 2021 during the dry season. In terms of vegetation, it is also observed that the Lamreh area is overgrown with trees that are resistant to dry soil conditions, i.e., java plum (*Syzygium cumini*) and jujube (*Ziziphus mauritiana).* They easily grow on a variety of infertile, wet, well-drained or dry soils [80].

The absence of water in this surface layer is also indicated by the chargeability value. Layers of sandy, silty and clayey with volcanic material and calcareous material have low chargeability values in desaturated conditions [81,82]. The water contained in the soil pores should be correlated with an increase in

chargeability, while in an empty condition the cavity is filled with air causing a low chargeability value [82]. However, the current density of the uppermost layer does not correlate well with the resistivity and chargeability values. Normally, materials with high resistivity should be characterized by low current density values. This layer cannot be detected by the VLF-EM method, since it is more sensitive to lateral changes in conductivity within the earth [77].

The layer which is characterized by moderate conductivity underneath is thought to be a calcareous sandstone layer as shown by the outcrop at the sea cliff walls (**Figure 5**). Water infiltration during rainfall through the uppermost layer pores is trapped in the sandstone layer so that this rock has a moderate resistivity value. In the IP model, although it is not sharply different, the layer can still be distinguished with a moderate chargeability value, which is around 10 msec. In the general case, the value of chargeability is directly proportional to the conductivity [83]. The lateral changes within the sandstone layer are caused by fractures or faults at several locations along the profiles. In the chargeability model, these are not clearly shown. Meanwhile, in the current density models, the fracture and fault locations are characterized by relatively high-density values [84] and are well connected with the findings in the resistivity models. The patterns of high current density values seen vertically are caused by the presence of water trapped in the sediments that fill the fractures and faults. Faults and fractures in rocks occur due to weathering. Weathering changes the chemical composition and physical properties of rocks [28].

The most conductive layer in the bottom is interpreted as breccia volcanic. On the cliff wall, the upper part of the breccia volcanic outcrop is still visible, but partly it is situated below sea level. Contact with salinity groundwater causes low resistivity values. With chargeability values of 12 - 15 msec, it is reasonable to interpret this rock as a water-saturated volcanic breccia [85]. The higher chargeability values could also be related to the unweathered rocks.

All models delineate the dipping of the layers towards the ends of both profiles. The dipping that occurs in the breccia and sandstone layers is subjected to weathering, erosional by a sea wave and gravitational effects. Weathering causes cracks in the rock body, and with the influence of gravitational force, the rock leans towards a lower position. The top surface of the sandstone layer could be associated with a sliding zone, resulting in avalanches of dry clastic sediments on the uppermost layer. Therefore, relatively thicker sediment accumulated at the ends of both profiles.

Seemly the resistivity, chargeability and current density contrasts in the models are not fully associated with lithological variations. They can be also related to mechanical weathering, saturation, and fracturing within the rocks. In terms of the electrical properties of a material, chemical and mechanical weathering are characterized by increasing resistivity [86]. It means the landslide that occurred in Lamreh could be associated with a highly deformed unsaturated material. Unsaturated alteration soil is characterized by high resistivity value due to low moisture content and medium chargeability. The unsaturated soils can trigger slope instability during the rainfall season. The slope instability occurs due to the presence of an additional shear strength within the unsaturated soil layer [87]. Rainwater seeps into the ground and affects the negative pore-water pressure.

Conclusions

This study has enriched information on the effectiveness of using the ERT, IP and VLF-EM methods in an integrated manner in investigating landslide-prone structures in cultural heritage areas as well as detailed subsurface information of the area study. In this case, the integrated geophysical method has been used to model the subsurface structure including lithological variations, the presence of faults and slip planes in the investigated area. The joint interpretation of the models generated from these geophysical methods has provided views from several perspectives based on the physical properties of each of the methods to provide a better understanding of the geological conditions below the surface. Geological variation of subsurface based on the type of lithology and water saturation in it can be well-characterized in the 2D ERT resistivity profiles. The ERT method was also able to clearly describe the slip plane as one of the conditions for triggering loose mass movements. The IP method was able to delineate layers based on water saturation and mineral content in it. While the VLF-EM method imaged lateral current density variations so that the location and depth of fractures or faults in the rock are known. Thus, the landslide-triggering aspects are well delineated under the studied area.

In addition to the reliable resolution of the resulting models, the electric current source injected into the soil in the ERT and IP methods as well as the electromagnetic wave source in the VLF-EM method did not cause damage to the cultural heritage site. Practically, the methods are considered straightforward, fast and cost-effective. For further development, it is necessary to improve measurement data space so that a better model resolution can be obtained. Join inversion of ERT, IP and VLF-EM data will also be able to

resolve subsurface structures more reliably. Repeated measurements at the location of the Lamreh cultural heritage site will also be able to provide a rate of mass movement in the area, thus stakeholders will be able to decide on mitigation and conservation efforts for the site appropriately.

Acknowledgements

This research was funded by the Universitas Syiah Kuala, Directorate of Higher Education, Ministry of Education and Culture, Indonesia, under Penelitian Unggulan Universitas (PUU) research grant with contract number 89/UN11.2.1/PT.01.03/PNBP/2022. The authors warmly thank Tomi Afrizal, Tarmizi, Badrul Munir, Agus Hari Pramana, Amir Asyqari, Syafrizal Idris and students from the Department of Geophysical Engineering and Department of Physics, Universitas Syiah Kuala, Indonesia for fieldwork logistical and technical assistance.

References

[1] EE McKinnon. Beyond serandib: A note on Lambri at the northern tip of Aceh. *Indonesia* 1988; **46**, 103-21.
[2] EE McKinnon. Aceh's defences. *Indonesia Malay World* 2009; **37**, 345-73.
[3] EE McKinnon. *Aceh and the maritime silk route: Aceh and Northern Sumatra, key locations on the ancient maritime silk route. In*: D Qin and J Yuan (Eds.). Ancient silk trade routes. Institute of Southeast Asian Studies, Singapore, 2015, p. 149-68.
[4] T Suarez. *Early mapping of Southeast Asia: The epic story of seafarers, adventurers, and cartographers who first mapped the regions between China and India*. Tuttle Publishing, Vermont, 2012.
[5] JN Miksic and GG Yian. *Ancient Southeast Asia*. Taylor & Francis, New York, 2016.
[6] RW Oetomo. Nisan plakpling, tipe nisan peralihan dari pra-islam ke islam. *Berkala Arkeologi Sangkhakala* 2007; **10**, 68-76.
[7] EE Mckinnon. *Continuity and change in South Indian involvement in Northern Sumatra: The inferences of archaeological evidence from Kota Cina and Lamreh. In*: PY Manguin, A Mani and G Wade (Eds.). Early interactions between South and Southeast Asia. ISEAS Publishing, Singapore, 2011, p. 137-60.
[8] A Husni, Saryulis, H Ibrahim and M Saidin. An investigation of archaeological remains at Lamreh site, Aceh, Indonesia and their context within the Lamuri kingdom. *Int. J. Asia Pac. Stud.* 2019; **15**, 59-88.
[9] D Satria. Batu nisan lamreh tipe 'plangpleng'. *Berkala Arkeologi Sangkhakala* 2019; **22**, 65-80.
[10] RM Feener, P Daly, E Edwards McKinnon, LL En-Ci, Ardiansyah, Nizamuddin, N Ismai, TY Seng, J Rahardjo and K Sieh. Islamisation and the formation of vernacular Muslim material culture in 15th century northern Sumatra. *Indonesia Malay World* 2021; **49**, 1-41.
[11] H Ibrahim, R Abdullah, S Hasyim, A Husni and M Saidin. Early islam of Lamuri site based on archaeological evidence. *Archaeol. Res. Asia* 2022; **29**, 100350.
[12] K Sieh, P Daly, EE McKinnon, JE Pilarczyk, HW Chiang, B Horton, CM Rubin, CC Shen, N Ismail, CH Vane and RM Feener. Penultimate predecessors of the 2004 Indian Ocean tsunami in Aceh, Sumatra: Stratigraphic, archeological, and historical evidence. *J. Geophys. Res. Solid Earth* 2015; **120**, 308-25.
[13] P Daly, EE McKinnon, RM Feener, TY Seng, Ardiansyah, A Parnell, Nizamuddin, N Ismail, K Sieh and J Majewski. The historic trading port of Lamri on the North Sumatran Coast. *Bulletin de l'École française l'Extrême-Orient* 2019; **105**, 115-44.
[14] P Daly, K Sieh, TY Seng and J Majewski. Archaeological evidence that a late 14th-century tsunami devastated the coast of northern Sumatra and redirected history. *Proc. Natl. Acad. Sci.* 2019; **116**, 11679-86.
[15] YS Tai, P Daly, EE Mckinnon, A Parnell, RM Feener, J Majewski, N Ismail and K Sieh. The impact of Ming and Qing dynasty maritime bans on trade ceramics recovered from coastal settlements in northern Sumatra, Indonesia. *Archaeol. Res. Asia* 2019; **21**, 100174.
[16] P Manguin, DES États, CD Asie, C De and PY Manguin. Histoire et archéologie des États côtiers de l' Asie du Sud-Est. *Annuaire de l'École Pratique des Hautes études* 1997; **11**, 223-5.
[17] A Hadi. *Aceh: Sejarah, budaya, dan tradisi*. Yayasan Pustaka Obor Indonesia, Jakarta, Indonesia, 2010.
[18] RM Feener. *Chapter I: The Acehnese past and its present state of study*. Mapping the Acehnese Past. Brill, Netherlands, 2011.

[19] D Perret. Aceh as a field for ancient history studies. *In*: Proceedings of the First International Conference of Aceh and Indian Ocean Studies, Banda Aceh, Indonesia. 2007, p. 1-11.
[20] DM Bridge, JD Bennett and NR Cameron. *Peta geologi lembar Banda Aceh, Sumatra. Geologic map of the Banda Aceh Quadrangle, Sumatra*. Direktorat Geologi, Bandung, Indonesia, 1981.
[21] Y Haditiar, MR Putri, N Ismail, ZA Muchlisin, M Ikhwan, M Ramli, S Sugianto, R Wafdan, MA Chaliluddin and S Rizal. The effect of monsoon on the bay of Bengal based on a hydrodynamic model. *J. Eng. Sci. Tech.* 2022; **17**, 936-55.
[22] M Zainal, M Yanis, D Darisma, Marwan and N Ismail. The determination of depth anomaly in archaeo-magnetic using an Euler deconvolution: Case study in Kuta Lubok fortress. *IOP Conf. Ser. Earth Environ. Sci.* 2019; **364**, 012034.
[23] EA Cherkez, OV Dragomyretska and Y Gorokhovich. Landslide protection of the historical heritage in Odessa (Ukraine). *Landslides* 2006; **3**, 303-9.
[24] T Xiao, DQ Li, ZJ Cao and XS Tang. Full probabilistic design of slopes in spatially variable soils using simplified reliability analysis method. *Georisk* 2017; **11**, 146-59.
[25] M Charrière, F Humair, C Froese, M Jaboyedoff, A Pedrazzini and C Longchamp. From the source area to the deposit: Collapse, fragmentation, and propagation of the Frank Slide. *GSA Bulletin* 2016; **128**, 922-30.
[26] JM Gasmo, H Rahardjo and EC Leong. Infiltration effects on stability of a residual soil slope. *Comput. Geotechnics* 2000; **26**, 145-65.
[27] A Bichler, P Bobrowsky, M Best, M Douma, J Hunter, T Calvert and R Burns. Three-dimensional mapping of a landslide using a multi-geophysical approach: The Quesnel Forks landslide. *Landslides* 2004; **1**, 29-40.
[28] D Jongmans and S Garambois. Geophysical investigation of landslides: A review. *Bulletin de la Société Géologique de France* 2007; **178**, 101-12.
[29] V Pazzi, S Morelli and R Fanti. A review of the advantages and limitations of geophysical investigations in landslide studies. *Int. J. Geophys.* 2019; **2019**, 2983087.
[30] JS Whiteley, JE Chambers, S Uhlemann, PB Wilkinson and JM Kendall. Geophysical monitoring of moisture-induced landslides: A review. *Rev. Geophys.* 2019; **57**, 106-45.
[31] VA Bogoslovsky and AA Ogilvy. Geophysical methods for the investigation of landslides. *Geophysics* 1977; **42**, 562-71.
[32] N Ismail, M Yanis, S Idris and F Abdullah. Near-surface fault structures of the seulimuem segment based on electrical resistivity model near-surface fault structures of the seulimuem segment based on electrical resistivity model. *J. Phys. Conf. Ser.* 2017; **846**, 012016.
[33] J Boyd, J Chambers, P Wilkinson, M Peppa, A Watlet, M Kirkham, L Jones, R Swift, P Meldrum, S Uhlemann and A Binley. A linked geomorphological and geophysical modelling methodology applied to an active landslide. *Landslides* 2021; **18**, 2689-704.
[34] TC Johnson, GE Hammond and X Chen. PFLOTRAN-E4D: A parallel open source PFLOTRAN module for simulating time-lapse electrical resistivity data. *Comput. Geosci.* 2017; **99**, 72-80.
[35] S Uhlemann, O Kuras, LA Richards, E Naden and DA Polya. Electrical resistivity tomography determines the spatial distribution of clay layer thickness and aquifer vulnerability, Kandal Province, Cambodia. *J. Asian Earth Sci.* 2017; **147**, 402-14.
[36] J Gallistl, M Weigand, M Stumvoll, D Ottowitz, T Glade and AF Orozco. Delineation of subsurface variability in clay-rich landslides through spectral induced polarization imaging and electromagnetic methods. *Eng. Geol.* 2018; **245**, 292-308.
[37] LD Slater and D Lesmes. IP interpretation in environmental investigations. *Geophysical* 2002; **67**, 77-88.
[38] A Revil, AS Ahmed, A Coperey, L Ravanel, R Sharma and N Panwar. Induced polarization as a tool to characterize shallow landslides. *J. Hydrol.* 2020; **589**, 125369.
[39] F Abdulsamad, A Revil, AS Ahmed, A Coperey, M Karaoulis, S Nicaise and L Peyras. Induced polarization tomography applied to the detection and the monitoring of leaks in embankments. *Eng. Geol.* 2019; **254**, 89-101.
[40] L Marescot, R Monnet and D Chapellier. Resistivity and induced polarization surveys for slope instability studies in the Swiss Alps. *Eng. Geol.* 2008; **98**, 18-28.
[41] AF Orozco, M Steiner, T Katona, N Roser, C Moser, MJ Stumvoll and T Glade. Application of induced polarization imaging across different scales to understand surface and groundwater flow at the Hofermuehle landslide. *Catena* 2022; **219**, 106612.
[42] GEM Systems. *GSM-19 v7.0 instruction manual release 7.4*. GEM Systems, Ontario, Canada, 2008.
[43] G Vargemezis. 3D geoelectrical model of geothermal spring mechanism derived from VLF

measurements: A case study from Aggistro (Northern Greece). *Geothermics* 2014; **51**, 1-8.
[44] WJ Phillips and WE Richards. A study of the effectiveness of the Vlf method for the location of narrow-mineralized fault zones. *Geoexploration* 1975; **13**, 215-26.
[45] D Beamish. Quantitative 2D VLF data interpretation. *J. Appl. Geophys.* 2000; **45**, 33-47.
[46] G Karcıoğlu. Near-surface resistivity structure near avcilar landslide in İstanbul, Turkey by 2D inversion of VLF data. *J. Appl. Geophys.* 2019; **163**, 73-83.
[47] M Yanis, MA Bakar and N Ismail. The use of VLF-EM and electromagnetic induction methods for mapping the ancient fort of Kuta Lubok as tsunami heritage i. *In*: Proceedings of the 23rd European Meeting of Environmental and Engineering Geophysics, Malmö, Sweden. 2017, p. 1-5.
[48] MA Khalil, FAM Santos, SM Moustafa and UM Saad. Mapping water seepage from lake nasser, Egypt, using the VLF-EM method: A case study. *J. Geophys. Eng.* 2009; **6**, 101-10.
[49] M Yanis, G Islami and N Ismail. Geophysics and geomorphic observation for near-surface structures mapping of Seulimeum Fault on Lamtamot area, Northern Sumatra. *Bull. Geol. Soc. Malaysia* 2022; **73**, 139-49.
[50] M Yanis, N Ismail and F Abdullah. Shallow structure fault and fracture mapping in Jaboi Volcano, Indonesia, using VLF-EM and electrical resistivity methods. *Nat. Resource Res.* 2022; **31**, 335-52.
[51] RW Oetomo. Metamorfose nisan Aceh, dari masa ke masa. *Berkala Arkeologi Sangkhakala* 2017; **19**, 130-48.
[52] Yunan. Situs kerajaan lamuri nyaris musnah, Available at: https://nasional.kompas.com/read/2013/01/03/21464922/~Sains~Arkeologi, accessed September 2022.
[53] M Nanda, S Rizal, F Abdullah, R Idroes and N Ismail. Mapping faults distribution based on dem data for regional spatial plan assessment of Sabang Municipality, Indonesia. *Int. J. Geomate* 2020; **19**, 197-204.
[54] M Chlieh, JP Avouac, V Hjorleifsdottir, TRA Song, C Ji, K Sieh, A Sladen, H Hebert, L Prawirodirdjo, Y Bock and J Galetzka. Coseismic slip and afterslip of the great Mw 9.15 Sumatra-Andaman earthquake of 2004. *Bull. Seismol. Soc. Am.* 2007; **97**, S152-S173.
[55] S Chapkanski, G Brocard, F Lavigne, C Tricot, E Meilianda, N Ismail, J Majewski, JP Goiran, D Alfian, P Daly, B Horton, A Switzer, V Degroot, A Steuer, B Siemon, J Cavero, C Virmoux and D Darusman. Fluvial and coastal landform changes in the Aceh River delta (northern Sumatra) during the century leading to the 2004 Indian Ocean tsunami. *Earth Surf. Proc. Landforms* 2022; **47**, 1127-46.
[56] Z Zhang, F Yang, H Chen, Y Wu, T Li, W Li, Q Wang and P Liu. GIS-based landslide susceptibility analysis using frequency ratio and evidential belief function models. *Environ. Earth Sci.* 2016; **75**, 948.
[57] J Efiong, DI Eni, JN Obiefuna and SJ Etu. Geospatial modelling of landslide susceptibility in Cross River State of Nigeria. *Sci. Afr.* 2021; **14**, e01032.
[58] K Tempa, K Peljor, S Wangdi, R Ghalley, K Jamtsho, S Ghalley amd P Pradhan. UAV technique to localize landslide susceptibility and mitigation proposal: A case of Rinchending Goenpa landslide in Bhutan. *Nat. Hazards Res.* 2021; **1**, 171-86.
[59] Badan Informasi Geospasial. *Seamless digital elevation model (DEM) dan batimetri nasional*. Geospatial Information Agency, West Java, Indonesia, 2018.
[60] BKP Horn. Hill shading and the reflectance map. *Proc. IEEE* 1981; **69**, 14-47.
[61] C Guillard and J Zezere. Landslide susceptibility assessment and validation in the framework of municipal planning in Portugal: The case of Loures Municipality. *Environ. Manag.* 2012; **50**, 721-35.
[62] RJ McGrath, P Styles, E Thomas and S Neale. Integrated high-resolution geophysical investigations as potential tools for water resource investigations in karst terrain. *Environ. Geol.* 2002; **42**, 552-7.
[63] FP Bosch and I Müller. Continuous gradient VLF measurements: A new possibility for high resolution mapping of karst structures. *First Break* 2001; **19**, 343-50.
[64] DC Fraser. Contouring of VLF-EM Data. *Geophysics* 1969; **34**, 958-67.
[65] DJ McNeill. *'Relacon', a VLF magnetic field 'relative conductivity' filter.* Geonics, Canada, 1991.
[66] M Pirttijarvi. *Manual of the KHFFILT program; Karous-Hjelt and Fraser filtering of VLF measurements, version 1.1a*. University of Oulu, Finland, 2004.
[67] H Reci, I Jata and S Bushati. The use of ERT method, for the detection of buried objects in archaelogical sites of Apollonia and Bylis, Albania. *Rom. Rep. Phys.* 2015; **67**, 665-72.
[68] A Binley and A Kemna. *DC resistivity and induced polarization methods. In*: Y Rubin and SS Hubbard (Eds.). Hydrogeophysics. Springer, Netherlands, 2005, p. 129-56.
[69] MH Loke. *Tutorial: 2-D and 3-D electrical imaging surveys*. Geotomo, Penang, Malaysia, 2002.
[70] MJ Starks, TF Bell, RA Quinn, US Inan, D Piddyachiy and M Parrot. Modeling of doppler-shifted

terrestrial VLF transmitter signals observed by Demeter. *Geophys. Res. Lett.* 2009; **36**, L12103.
[71] NR Thomson, MA Clilverd and CJ Rodger. Very low latitude whistler-mode signals: Observations at three widely spaced latitudes. *J. Geophys. Res. Space Phys.* 2019; **124**, 9253-69.
[72] Ministry of Environment and Forestry, Republic of Indonesia. *The state of Indonesia's forests 2018*. Ministry of Environment and Forestry, Republic of Indonesia, Indonesia, 2018.
[73] MD McCoy, GP Asner and MW Graves. Airborne lidar survey of irrigated agricultural landscapes: An application of the slope contrast method. *J. Archaeol. Sci.* 2011; **38**, 2141-54.
[74] H Kaur, S Gupta, S Parkash and R Thapa. Knowledge-driven method: A tool for landslide susceptibility zonation (LSZ). *Geol. Ecol. Landscapes* 2018; **7**, 1-15.
[75] Y Jeng, MJ Lin, CS Chen and YH Wang. Noise reduction and data recovery for a VLF-EM survey using a nonlinear decomposition method. *Geophysics* 2007; **72**, F223-F235.
[76] VR Babu, S Ram and N Sundararajan. Modeling and inversion of magnetic and VLF-EM data with an application to basement fractures: A case study from Raigarh, India. *Geophysics* 2007; **72**, B133-B140.
[77] P Gnaneshwar, A Shivaji, Y Srinivas, P Jettaiah and N Sundararajan. Very-low-frequency electromagnetic (VLF-EM) measurements in the Schirmacheroasen area, East Antarctica. *Polar Sci.* 2011; **5**, 11-9.
[78] FAM Santos, A Mateus, J Figueiras and MA Gonçalves. Mapping groundwater contamination around a landfill facility using the VLF-EM method - a case study. *J. Appl. Geophys.* 2006; **60**, 115-25.
[79] M Karous and SE Hjelt. Linear filtering of VLF dip - angle measurements. *Geophys. Prospect.* 1983; **31**, 782-94.
[80] S Dalimartha. *Atlas tumbuhan obat Indonesia*. Trubus Agriwidya, Jakart, Indonesia, 2003.
[81] G Okay, P Cosenza, A Ghorbani, C Camerlynck, J Cabrera, N Florsch and A Revil. Localization and characterization of cracks in clay-rocks using frequency and time-domain induced polarization. *Geophys. Prospect.* 2013; **61**, 134-52.
[82] D Mao, A Revil and J Hinton. Induced polarization response of porous media with metallic particles-part 4: Detection of metallic and nonmetallic targets in time-domain-induced polarization tomography. *Geophysics* 2016; **81**, D359-D375.
[83] A Revil, T Tartrat, F Abdulsamad, A Ghorbani and A Coperey. Chargeability of porous rocks with or without metallic particles. *Petrophysics* 2018; **59**, 543-52.
[84] M Nanda, S Rizal, F Abdullah, I Rinaldi and N Ismail. Near surface electrical resistivity structures around an active fault trace in Weh island, Indonesia. *Songklanakarin J. Sci. Tech.* 2021; **43**, 1152-9.
[85] MSE Juanah, S Ibrahim, WNA Sulaiman and PA Latif. Groundwater resources assessment using integrated geophysical techniques in the southwestern region of Peninsular Malaysia. *Arabian J. Geosci.* 2013; **6**, 4129-44.
[86] H Jomard, T Lebourg, Y Guglielmi and E Tric. Electrical imaging of sliding geometry and fluids associated with a deep seated landslide (La Clapière, France). *Earth Surf. Process. Landforms* 2010; **35**, 588-99.
[87] H Rahardjo, Y Kim and A Satyanaga. Role of unsaturated soil mechanics in geotechnical engineering. *Int. J. Geo Eng.* 2019; **10**, 8.